Journal of Alloys and Compounds 861 (2021) 158567

Contents lists available at ScienceDirect

Journal of Alloys and Compounds

journal homepage: www.elsevier.com/locate/jalcom

Magnetism and DFT calculations for understanding magnetic ground state of Fe doped Mn_2O_3

Renan A.P. Ribeiro[a,b,*], Marisa C. Oliveira[c], Elson Longo[b], Sergio R. de Lazaro[d], R. Nikam[e], P.S. Goyal[e], S. Radha[f], S. Rayaprol[g]

[a] Department of Chemistry, State University of Minas Gerais, Av. Paraná, 3001, 35501-170 Divinópolis, MG, Brazil
[b] CDMF-UFSCar, Universidade Federal de São Carlos, PO Box 676, 13565-905 São Carlos, SP, Brazil
[c] LSQM, Laboratório de Síntese Química de Materiais, DEMat, Universidade Federal do Rio Grande do Norte - UFRN, P.O. Box 1524, 59078-970 Natal, RN, Brazil
[d] Department of Chemistry, Av. Gen. Carlos Cavalcanti, nº 4748, 84030-000 Ponta Grossa, Paraná, Brazil
[e] Department of Physics, Pillai College of Engineering, New Panvel, Navi Mumbai 410206, India
[f] Department of Physics, University of Mumbai, Vidyanagari, Santacruz, Mumbai 400098, India
[g] UGC, DAE Consortium for Scientific Research, Mumbai Centre, B. A. R. C. Campus, Trombay, Mumbai 400085, India

ARTICLE INFO

Article history:
Received 16 September 2020
Received in revised form 23 December 2020
Accepted 28 December 2020
Available online 31 December 2020

Keywords:
DFT
Magnetism
Fe-doping
Mn_2O_3
Experimental

ABSTRACT

In the present work, we have carried out experimental analysis along with first-principles density functional theory (DFT) calculations to understand the magnetic ground state of Fe doped Mn_2O_3. The analysis of structural properties show that the orthorhombic type of crystal structure with space group *Pcab* is preserved, but the unit cell volume decreases with an increase in Fe concentration. Magnetic susceptibility measurements show that two antiferromagnetic transitions (T_{N1} = 25 K, T_{N2} = 80 K) for undoped Mn_2O_3 merged into one at around 35 K with increasing concentration of Fe doping ($Mn_{2-x}Fe_xO_3$; x = 0; 0.20; 0.50; 0.75). M-H curve at 5 K exhibits small hysteresis around the origin. The magnitude of magnetization increases with the increasing concentration of Fe. M-H curve at 100 K shows the linear behavior of M concerning H for x = 0.20 and x = 0.50, indicating the paramagnetic state of the sample. As a complement to the experimental analysis, first-principles calculations using DFT were carried out. Fe doping was simulated by the corresponding substitution of Mn atoms to reproduce stoichiometric features of $Mn_{2-x}Fe_xO_3$. The agreement between the two approaches suggests that the magnetic ground state of Fe doped Mn_2O_3 is tunable with Fe concentration.

1. Introduction

In the recent past, manganese oxides have received significant attention due to its applications in diverse fields such as catalysts in various environmental applications, electrodes in batteries, fuel cells, supercapacitors, electrochemical sensors, molecular adsorption, etc. [1–3]. Manganese oxides are found to have multifaceted functionality as it exhibits different structures and phases having different oxidation states (+2, +3, +4) due to various experimental conditions and with changing compositions [4,5]. Undoped Mn_2O_3 crystallizes into the orthorhombic structure with space group *Pcab* at room temperature [6] and undergoes orthorhombic to cubic transition at around 308 K [7,8]. The effect of substitution has many exciting effects on various structural, magnetic, and dielectric properties of Mn_2O_3 [9,10]. Keeping these attractive prospects in mind, we investigate the structural and magnetic properties of the $Mn_{2-x}Fe_xO_3$ (x = 0.0; 0.20; 0.50; 0.75) materials from the experimental and theoretical viewpoints.

2. Methodologies

2.1. Experimental details

2.1.1. Sample preparation

Polycrystalline samples of $Mn_{2-x}Fe_xO_3$ (x = 0; 0.20; 0.50; 0.75) were prepared by following the mechanochemical synthesis method [11,12]. Stoichiometric quantities of starting materials, MnO_2 and Fe_2O_3 (both with purities better than 99.9%) were taken in tungsten carbide (WC) jars along with 10 mm WC balls (in 1 g to 10 balls ratio) and ball milled for a total of 18 h at 400 rpm (main disk) speed. The samples were homogenized by heating in air at 825 °C for 72 h.

* Corresponding author at: Department of Chemistry, State University of Minas Gerais, Av. Paraná, 3001, 35501-170 Divinópolis, MG, Brazil.
E-mail addresses: renan.ribeiro@uemg.br, ribeiroapr@gmail.com (R.A.P. Ribeiro).

https://doi.org/10.1016/j.jallcom.2020.158567
0925-8388/

Finally, the resultant powder was cold pressed into pellets of 10 mm diameter and sintered again for 24 h at 825 °C.

2.1.2. Sample characterization

Samples were characterized for phase formation and structural properties by analyzing the X-ray diffraction patterns recorded at room temperature. Magnetic properties were measured as a function of temperature (susceptibility) and field (magnetization) on a commercial vibrating sample magnetometer (VSM) coupled to a physical property measurement system (M/s. Quantum Design-PPMS-VSM, USA).

2.2. Computational details

Aiming to disclose the structural, magnetic and electronic properties of Fe-doped $Mn_{2-x}Fe_xO_3$ oxides (x = 0; 0.25; 0.50; 0.75), first-principles calculations in the framework of the Density Functional Theory were carried out using PBE0 exchange-correlation functional implemented in CRYSTAL17 code [13,14]. At room temperature, pure Mn_2O_3 crystallizes in the cubic (*Ia3*) bixbyite-type structure named α-Mn_2O_3. However, other phases can be obtained depending on pressure and temperature conditions, such as orthorhombic β-Mn_2O_3 (*Pbca*), spinel-like γ-Mn_2O_3 (*I4$_1$/amd*), CaIrO_3-type phase δ-Mn_2O_3, corundum-type ε-Mn_2O_3 (*R-3c*), and perovskite-type structure of ζ-Mn_2O_3 (*P-1*) [15]. Here, orthorhombic β-Mn_2O_3 (*Pbca*) was confirmed as the stable polymorph for pure and Fe-doped samples. In this case, five non-equivalent Mn (Mn1–5) atoms centering [MnO_6] clusters, as depicted in Fig. 1a, can describe the crystalline structure, being the multiplicity of Mn(1,2) equals to 4, while Mn(3–5) sites exhibit multiplicity of 8, resulting in 32 Mn atoms at the conventional unit cell. Therefore, the Fe doping was modelled considering the substitution of 4 (x = 0.25), 8 (x = 0.5), (x = 0.75), and 12 Mn atoms in order to reproduce the experimental $Mn_{2-x}Fe_xO_3$ oxides (x = 0; 0.25; 0.50 and 0.75) stoichiometry, as presented in the Fig. 1b-d. Similar approaches were used in previous theoretical studies involving solid solutions showing a good agreement with experimental results [16].

The convergence criteria for mono- and bielectronic integrals were both set to 10^{-8} Hartree, while the RMS gradient, RMS displacement, maximum gradient, and maximum displacement were set to 3×10^{-5}, 1.2×10^{-4}, 4.5×10^{-5}, and 1.8×10^{-4} a.u., respectively. Regarding the density matrix diagonalization, the reciprocal space net was described by a shrinking factor set to 4 × 4×4, corresponding to 27 *k*-points following the Monkhorst-Pack method [17]. The accuracy in evaluating the Coulomb and exchange series was controlled by five thresholds, for which adopted values are 10^{-8}, 10^{-8}, 10^{-8}, 10^{-8}, and 10^{-16}. In all calculations, Mn atoms were described by effective-core pseudopotentials, while all-electron 86–411d41G and 8–411 basis set described Fe and O atoms [18,19].

Regarding the magnetic ground state, we consider two collinear magnetic configurations (FEM and AFM) using the optimized unit cell for $Mn_{2-x}Fe_xO_3$ oxides. In this case, the AFM model proposed for Mn_2O_3 by Cockayne and co-authors [20]. The magnetic ground state was defined as considered the energy difference between the models ($\Delta E = E_{AFM} - E_{FEM}$). This approach has reached good performance in magnetic oxides previously investigated [9,21,22]. Besides, the electronic properties were evaluated through Density of States (DOS), Band Structure profiles, and charge analysis tools implemented in the CRYSTAL17 code [13].

3. Results and discussions

3.1. X-ray diffraction

Fig. 2 shows the X-ray diffraction (XRD) patterns for the three synthesized compounds. For comparative purpose, XRD data for the α-Mn_2O_3 sample, simulated from the ICSD database (ICSD # 9090), is plotted along with the experimental data of $Mn_{2-x}Fe_xO_3$ (x = 0.20, 0.50, and 0.75) samples. All the samples were indexed in the orthorhombic structure, *Pbca* space group.

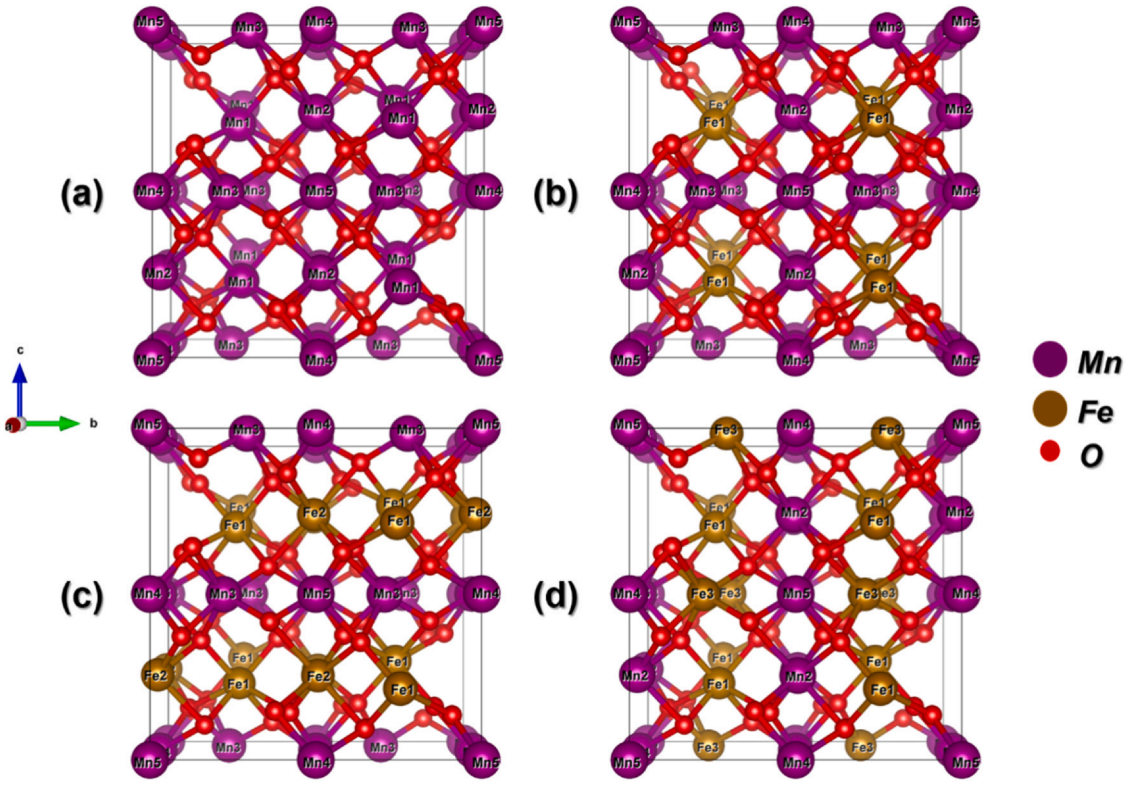

Fig. 1. *Pbca* conventional unit cell for (a) Mn_2O_3, (b) $Fe_{0.25}Mn_{1.75}O_3$, (c) $Fe_{0.50}Mn_{1.50}O_3$ and (d) $Fe_{0.75}Mn_{1.25}O_3$ materials.

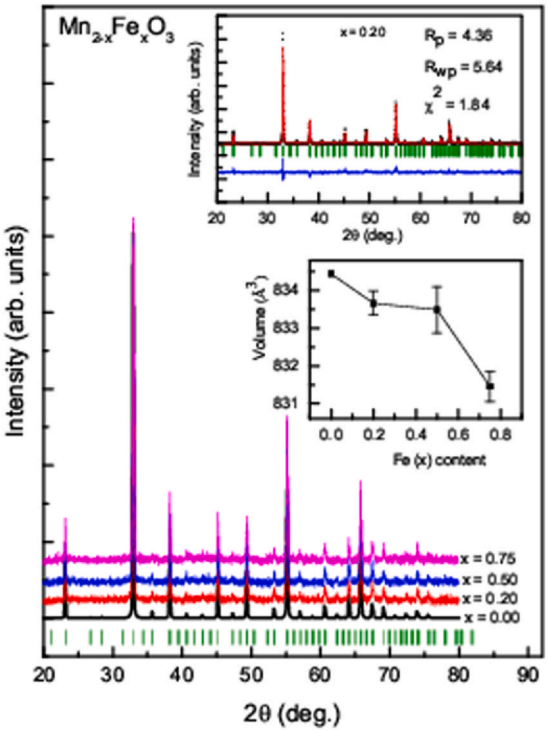

Fig. 2. X-ray diffraction patterns for $Mn_{2-x}Fe_xO_3$ samples recorded at room temperature. The top inset shows the Rietveld refinement of the XRD data for $Mn_{1.8}Fe_{0.2}O_3$. The raw data (black data points) and the simulated pattern (continuous red line) are shown with their difference pattern (continuous blue line) and expected Bragg peak positions (green colored vertical tick lines).(For interpretation of the references to colour in this figure legend, the reader is referred to the web version of this article.)

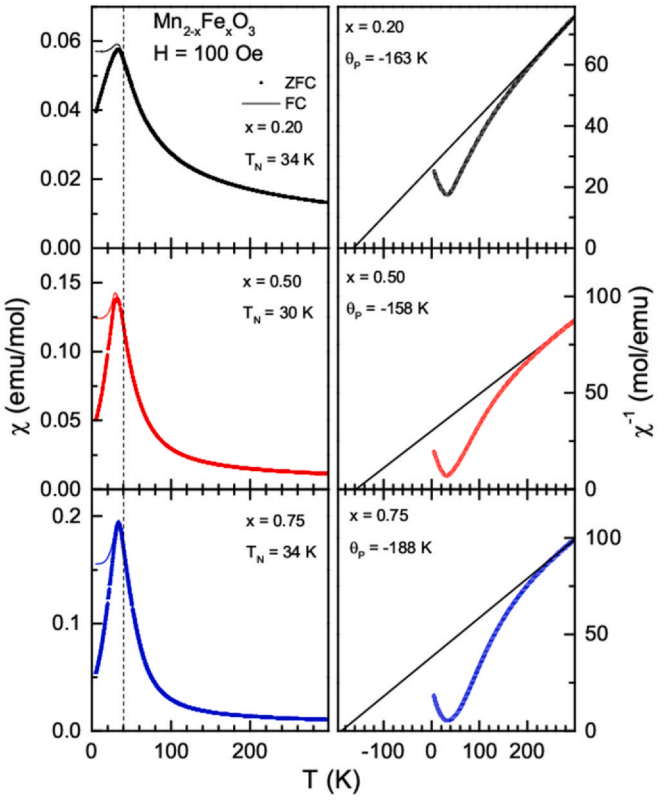

Fig. 3. Magnetic susceptibility ($\chi = M/H$) as a function of temperature for $Mn_{2-x}Fe_xO_3$ ($x = 0.2$, 0.5, and 0.75) measured while warming in the applied field of 100 Oe after cooling the sample in zero-field and in-field. In the right panels, the straight line is extended to show the θ_p values obtained from the fit to the Curie-Weiss law.

Table 1
Theoretical and experimental lattice parameters (in Å) and unit cell volume (in $Å^3$) in *Pbca* group for $Mn_{2-x}Fe_xO_3$ ($x = 0$; 0.20; 0.50; 0.75) materials.

System		a	b	c	V
Mn_2O_3	*Exp.*	9.415	9.423	9.404	834.451
	DFT/PBE0	9.431	9.468	9.391	838.599
$Mn_{1.80}Fe_{0.20}O_3$	*Exp.*	9.414	9.410	9.411	833.665
	DFT/PBE0 (x = 0.25)	9.435	9.488	9.360	837.934
$Mn_{1.50}Fe_{0.50}O_3$	*Exp.*	9.411	9.410	9.411	833.491
	DFT/PBE0	9.432	9.434	9.410	837.325
$Mn_{1.25}Fe_{0.75}O_3$	*Exp.*	9.408	9.407	9.395	833.601
	DFT/PBE0	9.458	9.480	9.336	837.120

The main panel of Fig. 2 exhibits the powder diffraction data plotted on the same scale (vertically lifted for the sake of clarity). The vertical tick marks below the pattern indicate the Bragg peak positions, while the first inset corresponds to the Rietveld refinement for the $Mn_{1.8}Fe_{0.2}O_3$ sample. On the other hand, in the second inset, the modification of unit cell parameter with respect to increasing Fe content is shown. Increasing Fe reduces the cell volume, indicating that Mn^{3+} (ionic radii = 0.58 Å) is replaced by Fe^{3+} (ionic radii = 0.55 Å). In Table 1, structural parameters obtained from the Rietveld refinement are given. The structural model used for the Rietveld analysis of the powder diffraction data is in good agreement with the model used for the theoretical calculations.

3.2. Magnetic properties

Earlier studies showed that Mn_2O_3 exhibits an antiferromagnetic ordering (AFM) around 80 K and 25 K [23]. In Fig. 3, the magnetic susceptibility (χ) for $Mn_{2-x}Fe_xO_3$ samples was measured applying a dc field of 100 Oe while warming after the sample was first zero-field cooled (ZFC) and then field-cooled (FC) in this field. It is interesting to note here that none of the three samples with Fe substitution shows ordering around 80 K. However, the magnetic ordering observed in these samples is in the 30 – 34 K range. It appears as if the lower T_N (~ 25 K) and the upper T_N (~ 80 K) observed in the pristine Mn_2O_3 have merged into one T_N ~ 34 K. These observations are consistent with the observations made for lower Fe doped orthorhombic Mn_2O_3 [23]. In this case, the magnetic ordering and its transition temperature is associated with the amount of distortion associated with the Fe-doping. Therefore, a magneto-structural effect is observed for doped Mn_2O_3, as described in the section containing the DFT calculations. With decreasing temperature, χ it increases and reaches a maximum around T_N and then falls with a further decrease in temperature. The fall is sharper in the ZFC state, and the difference between ZFC and FC starts appearing around T_N. The magnitude of susceptibility (in emu/mol) increased from Fe amount. For $x = 0.20$ and $x = 0.75$ samples, the ordering temperature (T_N) is around 34 K; and the $x = 0.50$ shows an ordering temperature lower 30 K. Similar trend is observed in the case of the paramagnetic Curie temperature (θ_p), which has been calculated using the Curie-Weiss law in the paramagnetic (linear) region of the inverse susceptibility. The frustration parameter given as $f = |\theta_p/T_N|$, shows increase from 4.8 for $x = 0.20$–5.5 for $x = 0.75$. Along with the values of θ_p and T_N it is seen that the Fe increase causes a magnetic frustration in the system.

Fig. 4 shows the measured magnetization for $Mn_{2-x}Fe_xO_3$ ($x = 0.20$, 0.50 and 0.75) samples at T = 5 K and 100 K. The M(H) for $x = 0.0$ sample exhibits an increase non-linear in M increasing H, and a small hysteresis in the magnetization. This result is connected to magnetic susceptibility, i.e., the magnitude of magnetization increases with an increase in Fe content is shown in the top panel of Fig. 4 (T = 5 K).

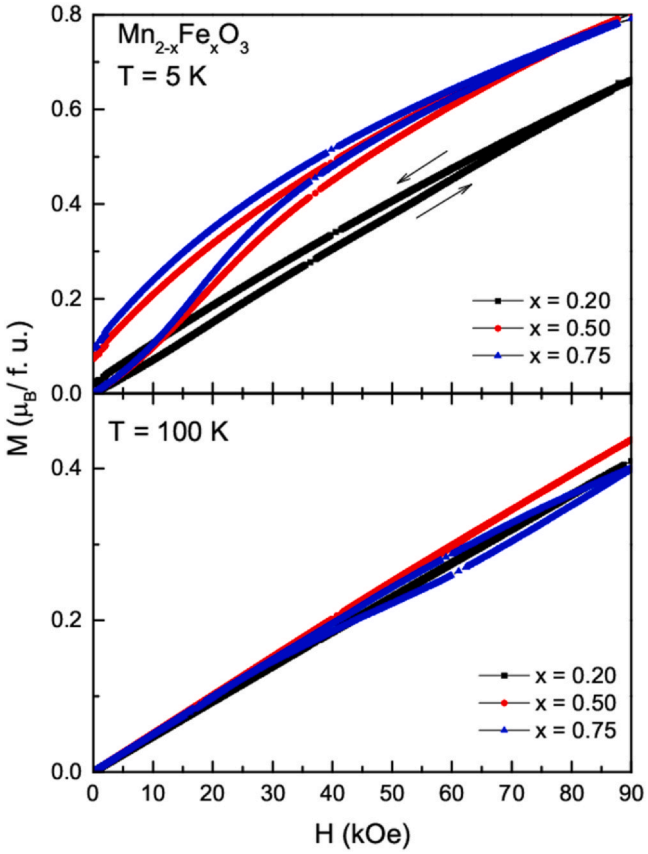

Fig. 4. Magnetization as a function of the applied magnetic field for $Mn_{2-x}Fe_xO_3$ (x = 0.20, 0.50 and 0.75) samples at T = 5 K (top panel) and 100 K (bottom panel). The arrow in the top panel indicates the (0 – 90 kOe – 0) direction.

For x = 0.50 and 0.75 at 5 K (Fig. 4), the M increases linearly with H, and then there is a non-linearly around 10 kOe. These features are not traced when the field is reduced to zero, existing a huge hysteresis around the origin. None sample presented saturations signature up to 90 kOe. M(H) measured at 100 K shows a linear behavior for x = 0.20 and 0.50, indicating a paramagnetic state. In the case of x = 0.75, M initially is linear with H (40 kOe); posteriorly, there is a spin-flop as a transition point. Then, the increases non-linearly with an increase in H (90 kOe). In M vs. H occurred a small loop for x = 0.75 between 40 kOe and 80 kOe. The down curve of the M(H) loop for x = 0.75 sample shows a non-linear behavior of M with H, indicating a possible induced magnetic field at short-range interaction or magnetic inhomogeneity in the sample.

3.3. DFT calculations

Here, it is essential to point out the main targets of the theoretical calculations were describing the Fe-doping role on the structural, magnetic, and electronic properties of the $Mn_{2-x}Fe_xO_3$ materials, i.e., a direct comparison between experimental and theoretical results. DFT/PBE0 simulations for $Mn_{2-x}Fe_xO_3$ (x = 0, 0.25, 0.50, 075) materials exhibited a reasonable agreement with experimental data for lattice parameters, being the use of effective-core pseudopotentials one of the possible reasons for the deviations (Table 1).

As regards the Fe-doping, theoretical results match with experimental evidence indicating a contraction of the unit cell volume for $Mn_{2-x}Fe_xO_3$ materials moving from x = 0.0 to x = 0.75. This fact can be discussed using the ionic radii of Mn^{3+} and Fe^{3+} cations, as well as the computed theoretical bond distances presented in the Supplementary Information (Table S1). In the six-fold coordination site, both Mn^{3+} and Fe^{3+} cations in low-spin configuration show ionic radii of 58 pm and 55 pm, respectively, justifying the minimal difference in the refined lattice parameters. Also, the electronic configurations associated with trivalent Mn^{3+} (d^4) and Fe^{3+} (d^5) cations show a singular spin distribution along the t_{2g} and e_g orbitals, i.e., the Fe^{3+} cations show $t_{2g}^3e_g^2$ distribution while Mn^{3+} cations present $t_{2g}^3e_g^1$ occupations. The odd number of electrons located at e_g orbital for Mn induces a Jahn-Teller disorder along the [MnO_6] clusters in comparison to [FeO_6] clusters. In this case, the doping of Fe on the Mn_2O_3 matrix induces shrinkage of neighboring Mn-O bonds because of the most regular character of [FeO_6] clusters, resulting in a slight unit cell contraction. These results can be associated with the merging of T_N temperatures through a magneto-structural behavior for Fe-doped Mn_2O_3 samples.

In order to obtain the magnetic ground state for $Mn_{2-x}Fe_xO_3$ (x = 0; 0.25; 0.50; 0.75) materials, collinear FEM and AFM models were considered based on the theoretical study developed by Cockayne and co-authors [20]. For pristine Mn_2O_3, calculated energy difference ($\Delta E = E_{AFM} - E_{FEM}$) indicates that AFM configuration is 4.05 meV/f.u. most stable in relation to FEM.

For $Mn_{2-x}Fe_xO_3$ (x = 0.25, 0.50, 0.75) materials the AFM model becomes a Ferrimagnetic (FIM) due to the different spin occupation of 3d orbitals for Mn^{3+} and Fe^{3+} centers. Further, doping with Fe, the calculated energy differences indicate that FIM ground state becomes more stable in comparison to the FEM configuration, once the relative energies were calculated as 21.97 meV/f.u., 36.85 meV/f.u. and 90.84 meV/f.u. for x = 0.25, x = 0.50 and x = 0.75, respectively. In all $Mn_{2-x}Fe_xO_3$ (x = 0.25; 0.50; 075) materials, the obtained ground state can be dissected in tree super-exchange paths: Mn-O-Mn, Fe-O-Fe, and Fe-O-Mn. In this case, the calculated coupling constant shows that Mn-Mn and Fe-Mn magnetic interactions are AFM, while Fe-Fe remains FEM, following the Goodenough-Kanamori-Anderson (GKA) rules. Here, it is important to point out that increasing the Fe amount the energy difference between magnetic structure becomes larger, which can be associated with the odd number of electrons located at e_g orbital for Mn that induces a Jahn-Teller disorder along the [MnO_6] clusters in comparison to [FeO_6] clusters, resulting in singular magnetic behaviors.

Aiming to explore the electronic structure of $Mn_{2-x}Fe_xO_3$ (x = 0; 0.25; 0.50; 0.75) materials, Density of States and Band Structure profiles were investigated. The electronic structure for pure Mn_2O_3 is presented in Fig. 5, indicating that the Valence Band (VB) is composed of Mn (3d) orbitals hybridized with O (2p) states, while empty states of Mn mainly compose the Conduction Band (CB). Besides, a direct band-gap of 2.96 eV was calculated between Γ-Γ points for the spin-beta channel, while the spin-up shows a higher energy

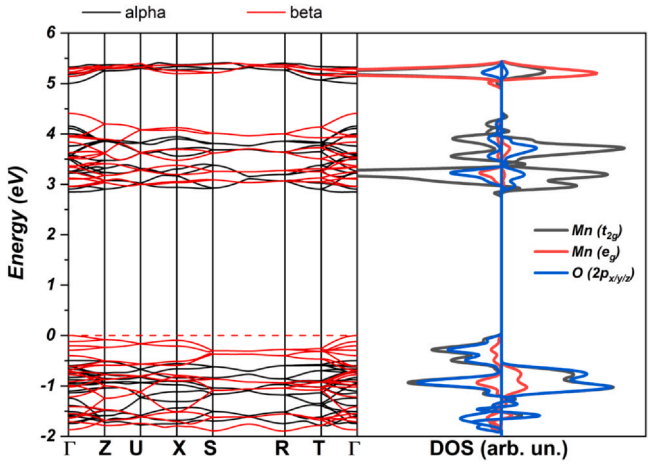

Fig. 5. Band Structure and orbital-resolved Density of States profiles for Mn_2O_3 material.

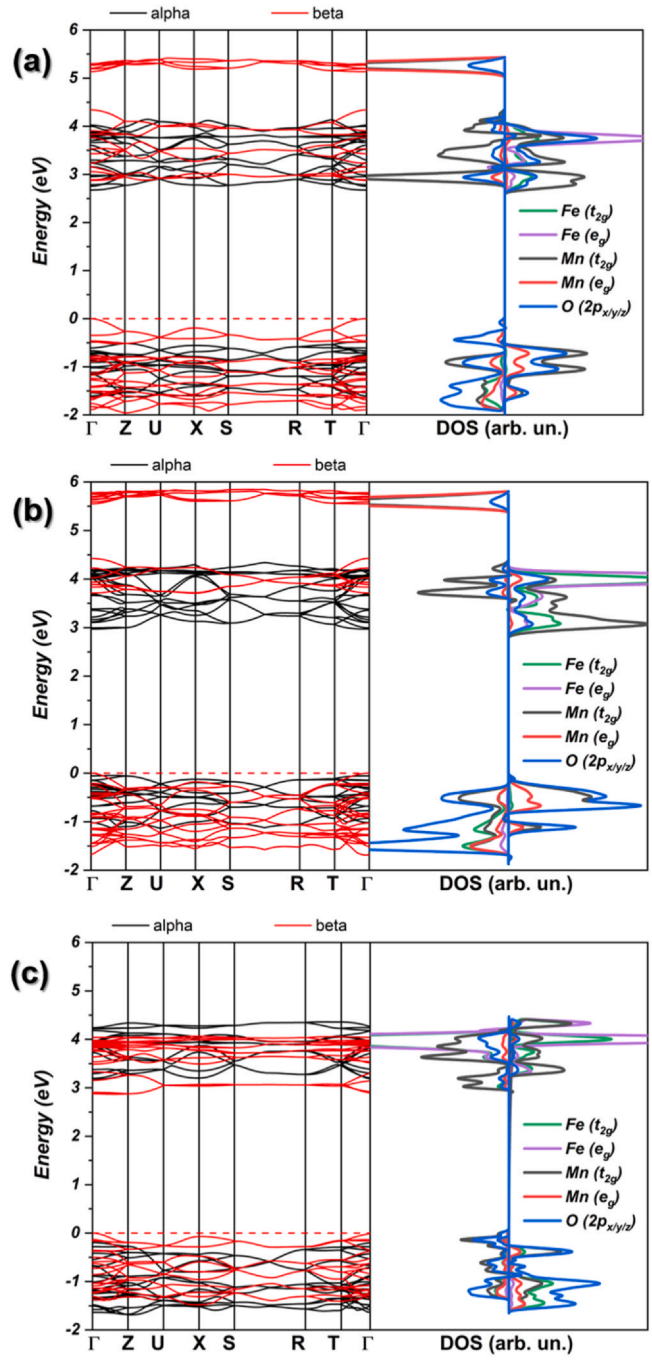

Fig. 6. Band structure and orbital-resolved Density of States profiles for (a) $Fe_{0.25}Mn_{1.75}O_3$, (b) $Fe_{0.50}Mn_{1.50}O_3$, and (c) $Fe_{0.75}Mn_{1.25}O_3$ materials.

excitation energy (3.35 eV), confirming the semiconductor behavior of Mn_2O_3.

Let us now briefly discuss the role of Fe-doping on the electronic structure of $Mn_{2-x}Fe_xO_3$ (x = 0.25; 0.50; 0.75) materials, as presented in Fig. 6.

In this case, it was noted that the composition of VB and CB was modified due to the insertion of Fe energy levels. For x = 0.20 (Fig. 6a), the obtained profiles indicate the inclusion of Fe (t_{2g}) energy levels mainly for the CB, reducing the band-gap to 2.87 eV between Γ-Γ points for the spin-beta channel, while the spin-up shows reduced band-gap energy (3.28 eV) in comparison to pure Mn_2O_3. For x = 0.50 (Fig. 6b), the obtained profiles indicate a major contribution of t_{2g} levels of Fe in both the lower part of VB and CB accompanied by a reduced direct (Γ-Γ) band-gap of 2.95 eV for the spin-up channel, while the opposite spin direction shows a large direct (Γ-Γ) band-gap of 3.69 eV in comparison to pure Mn_2O_3. Last but not least, for x = 0.75 (Fig. 6c), the inclusion of Fe orbitals in both VB and CB acts as intermediary energy levels in the band-gap region, reducing the band-gap to 2.91 eV for the spin-down channel, while the spin-up channel shows a large band-gap of 3.49 eV, both direct between Γ-Γ points. Therefore, the calculated band-gap order in beta channel indicates that $Fe_{0.25}Mn_{1.75}O_3$ (2.87 eV) < $Fe_{0.75}Mn_{1.25}O_3$ (2.91 eV) < $Fe_{0.50}Mn_{1.50}O_3$ (2.95 eV) < Mn_2O_3 (2.96 eV). The obtained results for Fe-doped models showed a smaller band-gap reduction in comparison to pure Mn_2O_3 due to the contribution of the t_{2g} orbitals of Fe from a structural disorder along with the crystalline structure that shrinkage the band-gap energy. Therefore, due to the few structural and electronic modifications, as well as magnetic ordering fluctuations, the change on T_N from Mn_2O_3 to Fe-doped samples can be associated with the existence of new Fe-O vibrational modes.

4. Conclusions

The $Mn_{2-x}Fe_xO_3$ (x = 0; 0.25; 0.50; 0.75) samples were synthesized in *Pcab* orthorhombic space group. Magnetic susceptibility measurements showed that Fe-doping samples have antiferromagnetic transitions around 35 K. M-H curves show that the magnetization magnitude increased from Fe-doping. The agreement between the two results suggests that the magnetic ground state for Fe-doped Mn_2O_3 is antiferromagnetic. The applied collinear DFT/PBE0 approach predicted with good performance the role of Fe-doping on the structural parameters of Mn_2O_3 due to the similarity of Mn^{3+} and Fe^{3+} ionic radii. The calculated band-gap results in the spin-down channel are near showing a low modification on electronic structure from Fe-doping. In particular, the theoretical calculations extend our understanding of the complex magnetic ordering for $Mn_{2-x}Fe_xO_3$ combining fundamental analysis based on the orbital occupation and crystalline structure arrangement in a magneto-structural viewpoint.

CRediT authorship contribution statement

Renan A. P. Ribeiro: Conceptualization of theoretical section, Formal analysis, Investigation, Writing - original draft, Writing - review & editing, Visualization. **Marisa C. Oliveira**: Conceptualization of theoretical section, Formal analysis, Investigation, Writing - review & editing, Visualization. **Elson Longo**: Writing - review & editing, Visualization, Project administration, Funding acquisition. **Sergio R. de Lazaro**: Writing - review & editing, Visualization, Supervision, Project administration. **R. Nikam**: Conceptualization of experimental section, Investigation, Writing - review & editing, Supervision, Project administration. **P. S. Goyal**: Conceptualization of experimental section, Investigation, Writing - review & editing, Supervision, Project administration. **S. Radha**: Writing - review & editing, Visualization, Project administration, Funding acquisition. **S. Rayaprol**: Writing - review & editing, Visualization, Project administration, Funding acquisition, Supervision, Project administration.

Declaration of Competing Interest

The authors declare that they have no known competing financial interests or personal relationships that could have appeared to influence the work reported in this paper.

Acknowledgments

This work was supported by the Federal University of São Carlos, the Federal University of Rio Grande do Norte (PPGCEM/UFRN), the

State University of Ponta Grossa (UEPG), CAPES, CNPq, and the Fundação Araucária (Brazil). R. A. P. Ribeiro acknowledges financial support from CNPq 156176/2018-1, as well as the National Laboratory for Scientific Computing (LNCC) and High-Performance Computing Center (NACAD) of the Federal University of Rio de Janeiro (COPPE-UFRJ) for providing the computational resources of Lobo Carneiro supercomputer. M. C. Oliveira acknowledges financial support from PNPD/CAPES (2019/88887.319041). E. Longo acknowledges financial support from FAPESP 2013/07296-2. The authors would like to thank Dr. V. Siruguri and Dr. P. D. Babu for magnetization data, M. Venugopal (CSR-Mumbai), for help in sample preparation, and Dr. Shovit Bhattacharya (TPD, BARC) for XRD measurements.

Appendix A. Supporting information

Supplementary data associated with this article can be found in the online version at doi:10.1016/j.jallcom.2020.158567.

References

[1] Y. Deng, Z. Li, Z. Shi, H. Xu, F. Peng, G. Chen, Porous Mn_2O_3 microsphere as a superior anode material for lithium ion batteries, RSC Adv. 2 (2012) 4645–4647.
[2] T. Yamashita, A. Vannice, NO Decomposition over Mn_2O_3 and Mn_3O_4, J. Catal. 163 (1996) 158–168.
[3] S. Sharma, Structural and optical properties of Mn_2O_3 nanoparticles & its gas sensing applications, Adv. Mater. Proc. 1 (2016) 220–225.
[4] R.K. Kunkalekar, A.V. Salker, Activity of Pd doped and supported Mn_2O_3 nanomaterials for CO oxidation, React. Kinet. Mech. Catal. 106 (2012) 395–405.
[5] P. Kar, S. Sardar, S. Ghosh, M.R. Parida, B. Liu, O.F. Mohammed, P. Lemmens, S.K. Pal, Nano surface engineering of Mn_2O_3 for potential light-harvesting application, J. Mater. Chem. C 3 (2015) 8200–8211.
[6] S. Geller, J.A. Cape, R.W. Grant, G.P. Espinosa, Distortion in the crystal structure of α-Mn_2O_3, Phys. Lett. A 24 (1967) 369–371.
[7] S. Geller, R.W. Grant, J.A. Cape, G.P. Espinosa, Magnetic structures in the α-Mn_2O_3–Fe_2O_3 system, J. Appl. Phys. 40 (1969) 1136.
[8] S. Geller, G.P. Espinosa, Magnetic and crystallographic transitions in Sc^{3+}, Cr^{3+}, Ga^{3+} substituted Mn_2O_3, Phys. Rev. B 1 (1970) 3763–3769.
[9] S. Rayaprol, R.A.P. Ribeiro, K. Singh, V.R. Reddy, S.D. Kaushik, S.R. de Lazaro, Experimental and theoretical interpretation of magnetic ground state of $FeMnO_3$, J. Alloy. Compd. 774 (2019) 290–298.
[10] S. Rayaprol, S.D. Kaushik, Magnetic and magnetocaloric properties of $FeMnO_3$, Ceram. Int. 41 (2015) 9567–9571.
[11] S. Rayaprol , S.D. Kaushik , P.D. Babu , V. Siruguri , A.K. Chauhan , C. Murli , S.C. Gadkari , Structure and magnetism of FeMnO3, AIP Conference Proceedings, 1512 (2013) 1132–1133.
[12] R. Nikam, S. Rayaprol, P.S. Goyal, P.D. Babu, S. Radha, V. Siruguri, Structural and magnetic properties of Fe-doped Mn_2O_3 orthorhombic bixbyite, J. Supercond. Noval Magn. 31 (2018) 2179–2185.
[13] R. Dovesi, A. Erba, R. Orlando, C.M. Zicovich-Wilson, B. Civalleri, L. Maschio, M. Rérat, S. Casassa, J. Baima, S. Salustro, B. Kirtman, Quantum-mechanical condensed matter simulations with CRYSTAL, Wires Comput. Mol. Sci. 8 (2018) e1360.
[14] C. Adamo, V. Barone, Toward reliable density functional methods without adjustable parameters: the PBE0 model, J. Chem. Phys. 110 (1999) 6158–6170.
[15] S.V. Ovsyannikov, A.M. Abakumov, A.A. Tsirlin, W. Schnelle, R. Egoavil, J. Verbeeck, G. Van Tendeloo, K.V. Glazyrin, M. Hanfland, L. Dubrovinsky, Perovskite-like Mn_2O_3: a path to new manganites, Angew. Chem. Int. Ed. 52 (2013) 1494–1498.
[16] M.C. Oliveira, J. Andrés, L. Gracia, M.S.M.P. de Oliveira, J.M.R. Mercury, E. Longo, I.C. Nogueira, Geometry, electronic structure, morphology, and photoluminescence emissions of $BaW_{1-x}Mo_xO_4$ (x = 0, 0.25, 0.50, 0.75, and 1) solid solutions: theory and experiment in concert, Appl. Surf. Sci. 463 (2019) 907–917.
[17] H.J. Monkhorst, J.D. Pack, Special points for Brillouin-zone integrations, Phys. Rev. B Condens. Matter Mater. Phys. 13 (1976) 5188–5192.
[18] M.D. Towler, N.L. Allan, N.M. Harrison, V.R. Saunders, W.C. Mackrodt, E. Aprà, Ab initio study of MnO and NiO, Phys. Rev. B 50 (1994) 5041–5054.
[19] M. Catti, G. Valerio, R. Dovesi, Theoretical study of electronic, magnetic, and structural properties of α-Fe_2O_3 (hematite), Phys. Rev. B 51 (1995) 7441–7450.
[20] E. Cockayne, I. Levin, H. Wu, A. Llobet, Magnetic structure of bixbyite α-Mn_2O_3: a combined DFT+U and neutron diffraction study, Phys. Rev. B 87 (2013) 184413.
[21] K. Manjunatha, V.J. Angadi, R.A.P. Ribeiro, M.C. Oliveira, S.R. de Lázaro, M.R.D. Bomio, S. Matteppanavar, S. Rayaprol, P.D. Babu, U.M. Pasha, Structural, electronic and magnetic properties of Sc^{3+} doped $CoCr_2O_4$ nanoparticles, N. J. Chem. 44 (2020) 14246–14255.
[22] K. Manjunatha, V. Jagadeesha Angadi, R.A.P. Ribeiro, E. Longo, M.C. Oliveira, M.R.D. Bomio, S.R. de Lázaro, S. Matteppanavar, S. Rayaprol, P.D. Babu, M. Pasha, Structural, electronic, vibrational and magnetic properties of Zn^{2+} substituted $MnCr_2O_4$ nanoparticles, J. Magn. Magn. Mater. 502 (2020) 166595.
[23] S. Geller, Structure of [alpha]-Mn_2O_3, $(Mn_{0.983}Fe_{0.017})_2O_3$ and $(Mn_{0.37}Fe_{0.63})_2O_3$ and relation to magnetic ordering, Acta Crystallogr. Sect. B 27 (1971) 821–828.